RSC Advances

PAPER

View Article Online
View Journal | View Issue

Cite this: *RSC Adv.*, 2024, **14**, 1538

Thermodynamic, electronic, and optical properties of ultra-wide bandgap zirconium-doped tin dioxide from a DFT perspective

Shan Peng, Xiaolin Wu, Yuanke Sun, Zhanxiang Zhou, Debing Long * and Huaqing Yu*

The effects of zirconium doping on the thermodynamic, electronic, and optical properties of tin dioxide are investigated by using density functional theory calculations combined with the cluster expansion method. In the whole composition range, the formation enthalpies of all structures are positive, indicating that SnO_2–ZrO_2 is an immiscible system and the $ZrSnO_2$ alloy has a tendency of phase separation at low temperature. The x-T phase diagram of $ZrSnO_2$ ternary alloy shows that the critical temperature is 979 K, which means that when the growth temperature of $ZrSnO_2$ crystal is higher than the critical temperature, it is possible to realize the full-component solid solution. The bandgaps of $Zr_xSn_{1-x}O_2$ alloys ($0 \leq x \leq 1$) are direct and increase as the Zr composition increases. Zr doping can tune the bandgap of SnO_2 from the ultraviolet-B region to the deep ultraviolet region, and has a strong optical response to deep ultraviolet light. The projected density of states and band offsets clearly reveal the reason for the increase of bandgap, which provides useful information to design relevant optoelectronic devices such as quantum wells and solar-blind deep ultraviolet photodetectors.

Received 17th December 2023
Accepted 19th December 2023

DOI: 10.1039/d3ra08607k

rsc.li/rsc-advances

1. Introduction

Semiconductor deep ultraviolet (UV) optoelectronic devices have great application prospects in the fields of the national economy and people's livelihoods, military defense, and other fields, and can be widely used in laser precision processing, precision measurement, semiconductor lithography processes, biomedicine, water and air detection and purification, heat source detection, *etc.*[1–3] Therefore, ultra-wide bandgap semiconductor materials with a band gap of more than 4.5 eV have gradually attracted the attention of researchers from all over the world. Common ultra-wide bandgap semiconductor materials include aluminum nitride (6.2 eV), diamond (5.5 eV), β-Ga_2O_3 (4.8 eV), SnO_2 (3.6 eV), *etc.* Although some progress has been made in the research of ultra-wide bandgap semiconductor materials, there are still some problems *e.g.* that the $Al_xGa_{1-x}N$ system is prone to phase separation and composition segregation under high Al content. At the same time, the donor and acceptor levels will become deeper and difficult to excite; due to the continuous photoconductivity effect, the response time of AlGaN-based UV photodetectors is difficult to improve.[4] High quality and large area epitaxial growth of diamond has been difficult, and there is no effective bandgap adjustment method. The p-type doping of β-Ga_2O_3 is very difficult due to its band structure.[5]

Due to the bandgap of 3.6 eV in SnO_2, it can be used as a UV-B band photodetector. F-doped SnO_2 has been widely used as a transparent conductive material in fields such as LEDs and solar cells.[6,7] Li *et al.* improved the luminous efficiency of SnO_2 by doping In in SnO_2, and achieved near UV electroluminescence at 398 nm.[8] At the same time, they also found that Ag doping can form acceptors and achieve near-band edge luminescence at 361–375 nm. In addition, the transformation of SnO_2 from n-type to p-type can be achieved by heavily doping Mg in SnO_2, and strong UV luminescence can be observed in photoluminescence experiments.[9,10] Xue *et al.* achieved ultra-wide response photodetectors in the 365 nm to 980 nm wavelength range by growing SnO_2 on p-type Si.[11] However, limited by the bandgap of SnO_2 (3.6 eV), the minimum cutoff wavelength of the above devices is about 320 nm, which can only achieve visible light-blind UV detection, and it is difficult to achieve solar-blind deep UV detection. In SnO_2, both 5s and 5p electrons of Sn are transferred to the O atom, resulting in empty bands of 5s and 5p, forming the conduction band minimum (CBM). The 4d band of Sn is in a full band state, located below the valence band maximum (VBM). The VBM of SnO_2 is composed of the 2p orbital of O. By doping Zr to partially replace Sn, the unfilled Zr-4d orbital and O-2p orbital are hybridized to form the VBM, thereby changing the symmetry of the VBM and achieving efficient optoelectronic conversion. In addition, the ionic radius of Zr^{4+} (0.79 Å) is slightly larger than that of Sn^{4+} (0.69 Å), hence the similar ionic radius means Zr^{4+} ions can easily replace Sn^{4+} ions in the crystal lattice, and the

School of Physics and Electronic-Information Engineering, Hubei Engineering University, Xiaogan, 432000, P. R. China. E-mail: dblong@hbeu.edu.cn; yuhuaqing@hbeu.edu.cn

product compound can stabilize the lattice structure. The bandgap of ZrO_2 (5–7 eV) is much wider than that of SnO_2, which is suitable for forming a ternary alloy with SnO_2, increasing the bandgap of SnO_2 and achieving band regulation, so as to realize its application in the field of ultra-short wavelength and deep UV photodetectors.

In this paper, the crystal structure, solubility limit, electronic and optical properties of $ZrSnO_2$ alloy are systematically studied by first-principles calculations combined with the cluster expansion method. The variation trend and regulation mechanism of the bandgap of the alloy caused by Zr doping are revealed. This will provide meaningful guidance and reference for the band engineering of SnO_2 and its potential application in solar-blind deep UV detectors in theory and technology.

2. Computational methodologies

The cluster expansion (CE) method is performed by the MIT *Ab initio* Phase Stability (MAPS) program in the Alloy Theoretic Automated Toolkit (ATAT)[12] to generate $Zr_xSn_{1-x}O_2$ alloy configurations with different doping contents, and quickly fit the energies of a small portion of configurations calculated by DFT to obtain the formation enthalpies for all configurations. The CE method has been successfully applied to the study of various alloy systems, such as PdH_x,[13] $Mg_xNi_{1-x}O$,[14] CdS_xSe_{1-x},[15] and $ZnS_{1-x}Se_x$.[16] In principle, the $Zr_xSn_{1-x}O_2$ alloy phase equilibrium and ground state calculations require one to determine the total energies of all possible configurations. However, it is costly and unrealistic to calculate the total energies of all possible configurations *via* first-principles calculations. An Ising-like Hamiltonian can be constructed *via* the CE method to determine the energies of different alloy configurations. It can rapidly calculate the energy of any alloy configuration and thus saves significant computation time. Here, we give a generalized description of the CE method. The Ising-like Hamiltonian for the energies of possible configurations σ is calculated using

$$E(\sigma) = J_0 + \sum_i J_i \hat{S}_i(\sigma) + \sum_{j<i} J_{ij} \hat{S}_i(\sigma)\hat{S}_j(\sigma) + \sum_{k<j<i} J_{ijk} \hat{S}_i(\sigma)\hat{S}_j(\sigma)\hat{S}_k(\sigma) + \cdots \quad (1)$$

where the J's (J_i, J_{ij}, J_{ijk}, *etc.*) denote the interaction energies (effective cluster interactions) and $\hat{S}_i$ ($i = 1, 2, \ldots, N$) are the "spin" variables. $\hat{S}_i$ take the value of +1 or −1 corresponding to the i site occupied by a Sn or Zr atom. The interaction energies J's are obtained by fitting the results of DFT calculations. In this work, 25 alloy configurations are calculated by DFT to obtain the interaction energies. Once the J's are obtained, the energy of any configuration can be rapidly computed using eqn (1). In the process of CE, the MAPS procedure is performed continuously by gradually increasing the number of clusters contained in the CE until the desired precision is reached. The predictive power of the CE method is controlled by the so-called cross-validation (CV) score, which is often defined by comparing the difference between the DFT-calculated energies E_i^{DFT} and the fitted energies E_i^{fit} from the CE method

$$CV = \left(\frac{1}{N} \sum_{i=1}^{N} \left(E_i^{DFT} - E_i^{fit} \right)^2 \right)^2 \quad (2)$$

A small CV score provides a basis for the power of the CE method. We can consider the CE to be suitable when a CV score of less than 100 meV per cation appears. In this work, the CV score is less than 0.73 meV per cation. We have added a detailed description of the CE method in the computational methodology section of the revised manuscript.

The structural relaxation and property characterization were performed using the first-principles calculation program Quantum Espresso.[17] The ultrasoft pseudopotentials (USPPs)[18] method was used to describe the interaction between ions and electrons, and the generalized gradient approximation in Perdew–Burke–Ernzerhof (PBE)[19] form was used as the exchange correlation function to handle the interaction between electrons. A plane wave energy cutoff of 600 eV was applied in the entire calculation. The convergence thresholds for energy and atomic forces in the self-consistent calculation were set to be less than 0.05 GPa and 1.4×10^{-5} eV, respectively. Due to strong onsite Coulomb interaction of Zr-4d orbital, the PBE+U strategy was adopted to describe the Coulomb and exchange correlation effects of Zr-4d orbital. An effective U value of 4 eV [20] produced ZrO_2 equilibrium lattice parameters of $a = b = 3.68$ Å and $c = 5.22$ Å, which are consistent with the experimental values of $a = b = 3.61$ Å and $c = 5.21$ Å.[21]

The branch-point energy (BPE) E_{BP} is regarded as an energy reference level for the band alignment in the band offset calculations.[22] It can be using

$$E_{BP} = \frac{1}{2N_k} \sum_k \left[\frac{1}{N_{CB}} \sum_i^{N_{CB}} \varepsilon_{c_i}(k) + \frac{1}{N_{VB}} \sum_j^{N_{VB}} \varepsilon_{v_j}(k) \right] \quad (3)$$

where N_k denotes the number of Γ-centered Monkhorst–Pack k points in the Brilloun zone. N_{CB} and N_{VB} represent the number of conduction bands (CBs) and valences bands (VBs) at Γ-centered Monkhorst–Pack k points, respectively, while $\varepsilon_{c_i}(k)$ and $\varepsilon_{v_j}(k)$ are the energies corresponding to the conduction bands and valence bands. In this work, the BPE is computed by averaging the eigenvalues of the two highest valence bands ($N_{VB} = 2$) and the lowest conduction band ($N_{CB} = 1$). Once the BPE is determined, it is set to zero and all DFT-calculated VBMs and CBMs refer to it. Then, the VBM and CBM band offsets for $Zr_xSn_{1-x}O_2$ alloys with different Zr contents can be obtained as follows:

$$\Delta E_v = \Delta E_{VBM} - \frac{1}{2} dE_g \quad (4)$$

$$\Delta E_c = \Delta E_{CBM} + \frac{1}{2} dE_g \quad (5)$$

where $dE_g = E_g^{\Delta\text{-sol}} - E_g^{GGA+U}$. In the above equation, $E_g^{\Delta\text{-sol}}$ and E_g^{GGA+U} indicate the band gaps determined using the Δ-sol and GGA+U methods, respectively.

The optical absorption coefficients are calculated based on the imaginary part $\varepsilon_2(\omega)$ of the frequency dependent complex dielectric function $\varepsilon(\omega) = \varepsilon_1(\omega) + i\varepsilon_2(\omega)$ to quantitatively

understand their light-harvesting ability. The imaginary part $\varepsilon_2(\omega)$ is first calculated according to the following formula:[23]

$$\varepsilon_2(\omega) = \frac{4\pi^2}{m^2\omega^2}\sum_{c,v}\int_{BZ}\frac{2}{(2\pi)^3}|M_{c,v}(k)|^2\delta(\varepsilon_{ck} - \varepsilon_{vk} - \hbar\omega)d^3k \quad (6)$$

where $|M_{c,v}(k)|^2$ denotes the momentum matrix element, and c and v are the conduction and valence band states, respectively. Then the real part $\varepsilon_1(\omega)$ is derived from the imaginary part according to the Kramers–Kroning transformation.[24] Finally, we can obtain the optical absorption coefficients $\alpha(\omega)$ *via* the following expression:[25]

$$\alpha(\omega) = \sqrt{2}\omega\left[\sqrt{\varepsilon_1^2(\omega) + \varepsilon_2^2(\omega)} - \varepsilon_1(\omega)\right]^{1/2} \quad (7)$$

3. Results and discussion

3.1. Thermodynamic properties

3.1.1. Formation enthalpy and ground-state search. Based on the 25 DFT calculated structures, 670 configurations with different distribution of dopants were searched through CE. Using CE, we estimated the formation enthalpies of all symmetrically independent configurations, accommodating up to 48 atoms in the supercell, as depicted in Fig. 1. Through ground state search, ground state structures are only found at two endpoints (SnO_2 and ZrO_2), with no other intermediate ground states (the stable $Zr_xSn_{1-x}O_2$ alloy configurations with other contents ($0 < x < 1$) with formation enthalpies below 0, except for $x = 0$ and 1) present. The formation enthalpies of all $Zr_xSn_{1-x}O_2$ alloy configurations are positive, indicating that SnO_2 and ZrO_2 are difficult to form stable and ordered alloy solid solutions. They exhibit a trend of phase separation at low temperatures, but may form good disordered alloys at high temperatures.

3.1.2. Phase diagrams. The thermodynamic phase diagram provides important clues for studying the solubility limit and phase transition temperature of alloys. The binodal curves (the equilibrium solubility limits) are formed *via* common tangent construction to the Gibbs free energy ΔG at a given temperature and the spinodal curves (the nonequilibrium metastability limits) are made up of the points where the second derivative of ΔG equals zero at a given T. The Gibbs free energy ΔG is defined by

$$\Delta G(x, T) = \Delta H(x, T) - T\Delta S(x) \quad (8)$$

Here, x is the concentration of Zr, ΔH is the formation enthalpy, and ΔS is the mixing entropy as described by the Bragg–Williams approximation.[26] The mixing entropy is given by $\Delta S = -k_B[x\log x + (1-x)\log(1-x)]$ per cation. T is the temperature. The binodal and spinodal curves in Fig. 2 divide the phase diagram into the stable, metastable and unstable mixing regions. In the region outside the binodal curve, the $Zr_xSn_{1-x}O_2$ solid solutions are single-phase, homogeneous, and stable. The metastable region exists between the binodal and spinodal curves. Phase separation occurs in the region inside the spinodal curve, where the $Zr_xSn_{1-x}O_2$ solid solutions are unstable. The critical temperature T_C of $ZrSnO_2$ alloy is 979 K, this means that above this temperature, the $ZrSnO_2$ alloy may achieve full-component solid solution. Through advanced semiconductor crystal growth technologies such as metal organic chemical vapor deposition (MOCVD), molecular beam epitaxy (MBE), and pulse laser deposition (PLD), the synthesis of stable $ZrSnO_2$ alloys at high temperatures can be achieved. At present, Zr:SnO_2 alloy thin films prepared by spray pyrolysis, chemical vapor deposition and Nb:$Zr_xSn_{1-x}O_2$ alloy films prepared by pulsed laser deposition have been reported in the experiment.[27–29] The preparation temperatures are 150–200, 400, and 720 °C, respectively. This indicates that $Zr_xSn_{1-x}O_2$ alloys are very promising to be prepared experimentally. The application of

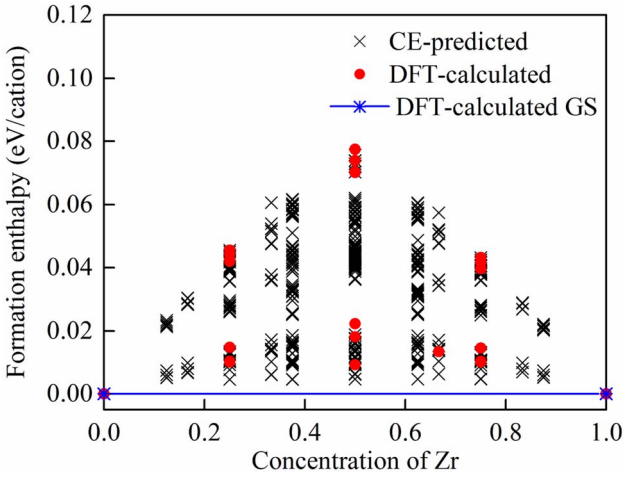

Fig. 1 Formation enthalpies of $Zr_xSn_{1-x}O_2$ alloys. Black crosses represent CE-predicted energies, red dots denote the DFT-calculated formation enthalpies of selected configurations, and stars mark the two end points SnO_2 and ZrO_2 as DFT-calculated ground states of $Zr_xSn_{1-x}O_2$.

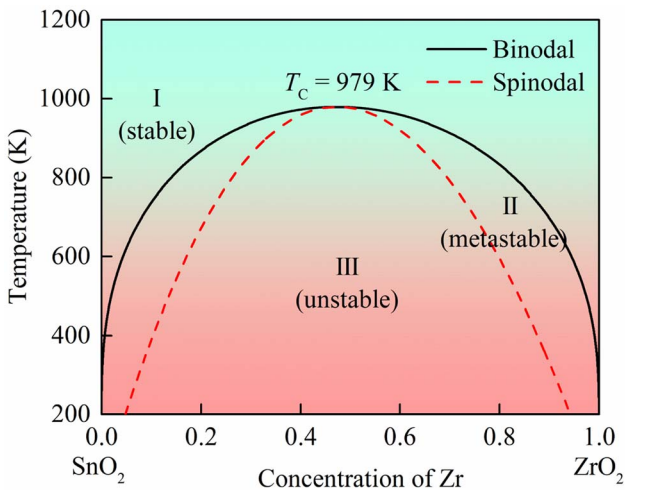

Fig. 2 The x-T phase diagram of $Zr_xSn_{1-x}O_2$ alloys. Solid and dotted lines represent the equilibrium binodal and spinodal curves, respectively.

semiconductor materials under high temperature or extreme conditions is also what people need. Therefore, the stable wide bandgap $ZrSnO_2$ alloys at high temperatures have practical application value and research significance.

3.2. Electronic properties

3.2.1. Band structures and density of states. To investigate the effect of Zr dopant concentration on the electronic structure, five low-lying configurations with different Zr contents (x = 0, 0.25, 0.5, 0.75, and 1) were select to analyze the variation of bandgap with composition. The crystal structures of five low-lying configurations are shown in Fig. 3. Due to the larger ion radius of Zr, the lattice constants of $Zr_xSn_{1-x}O_2$ alloys monotonically increase with the increment of Zr content, as listed in Table 1. The cohesive energies E_c of $Zr_xSn_{1-x}O_2$ alloys are calculated using the following formula:

$$E_c = \frac{16xE_{Zr} + 16(1-x)E_{Sn} + 32E_O - E_{Zr_xSn_{1-x}O_2}}{48} \quad (9)$$

where $E_{Zr_xSn_{1-x}O_2}$ is the total energy of the $Zr_xSn_{1-x}O_2$ alloy, and E_{Zr}, E_{Sn}, and E_O are the energies of an isolated Zr, Sn, and O

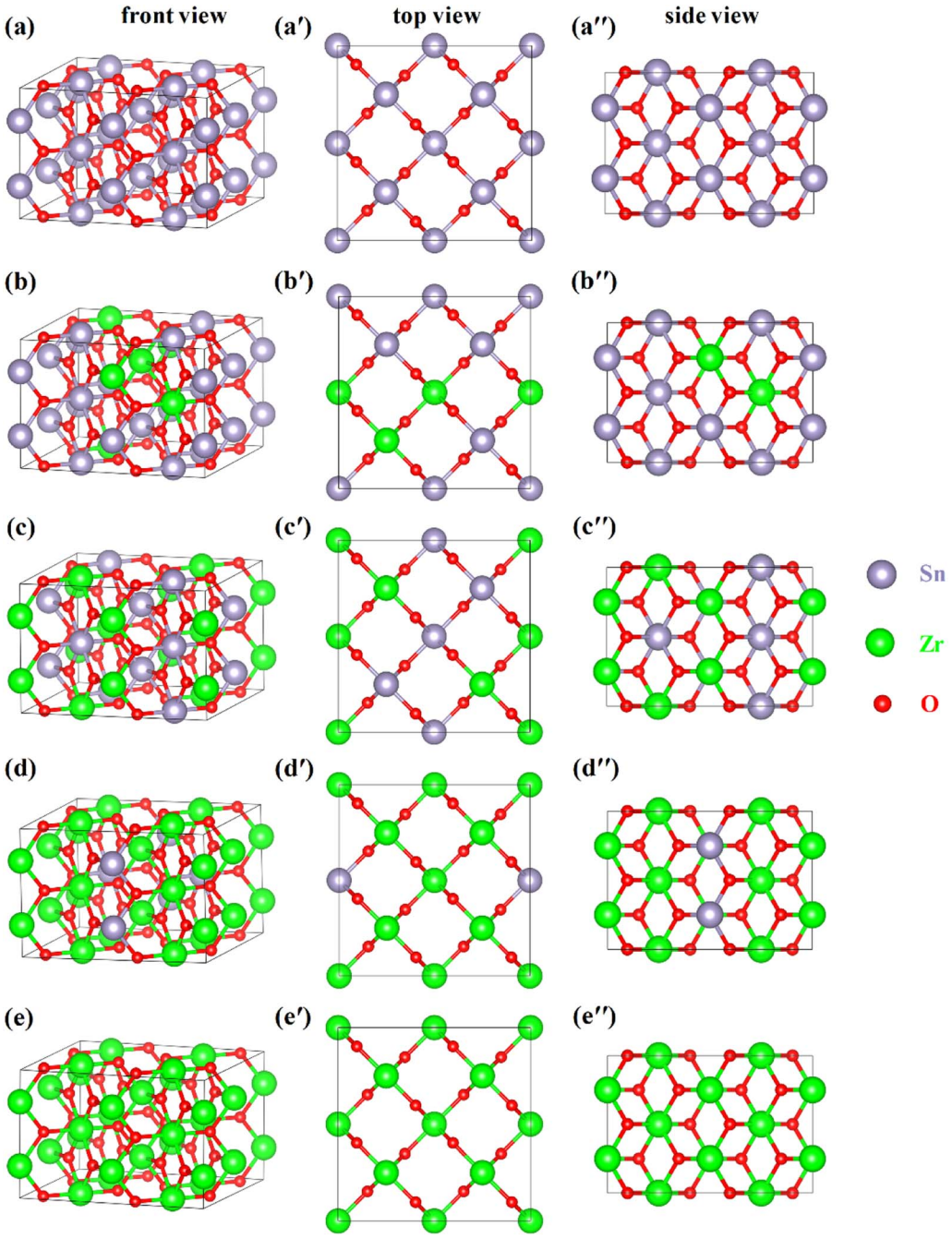

Fig. 3 The front views of (a) SnO_2, (b) $Zr_{0.25}Sn_{0.75}O_2$, (c) $Zr_{0.5}Sn_{0.5}O_2$, (d) $Zr_{0.75}Sn_{0.25}O_2$, and (e) ZrO_2. (a′)–(e′) and (a″)–(e″) are the corresponding top and side views in (a)–(e), respectively. The brown, green, and red balls are Sn, Zr, and O atoms, respectively.

Table 1 Crystal structure information and cohesive energies (E_c) of $Zr_xSn_{1-x}O_2$ (x = 0, 0.25, 0.5, 0.75, and 1) alloys

$Zr_xSn_{1-x}O_2$	a (Å)	b (Å)	c (Å)	α (°)	β (°)	γ (°)	E_c (eV per atom)
0	9.61	9.61	6.46	90	90	90	5.13
0.25	9.65	9.65	6.49	89.91	89.99	90.03	5.84
0.5	9.68	9.72	6.49	90	90	90.01	6.57
0.75	9.73	9.74	6.50	90	90	89.99	7.28
1	9.77	9.77	6.52	90	90	90	8.01

atom in vacuum, respectively. It can be seen that these $Zr_xSn_{1-x}O_2$ alloys have high cohesive energies, indicating that they can theoretically form stable ternary compounds. In addition, it is worth noting that due to the different ionic radii between Zr and Sn atoms, the lattice constants and α, β, γ angles of SnO_2 undergo small changes, resulting in lattice distortion, which leads to an orthogonal or monoclinic lattice symmetry in the $Zr_xSn_{1-x}O_2$ alloy configuration.

The calculated band structures are shown in Fig. 4, and it can be seen that the VBMs and CBMs of $Zr_xSn_{1-x}O_2$ alloys are both located at the Γ point in the Brillouin zone. Therefore, these $Zr_xSn_{1-x}O_2$ alloys are direct bandgap semiconductors. As the Zr content increases, the bandgap shows a monotonically increasing trend, with bandgap value ranging from 0.72 to 3.91 eV, as shown in Fig. 5. The distribution of the valence bands is less dispersed than that of the conduction bands

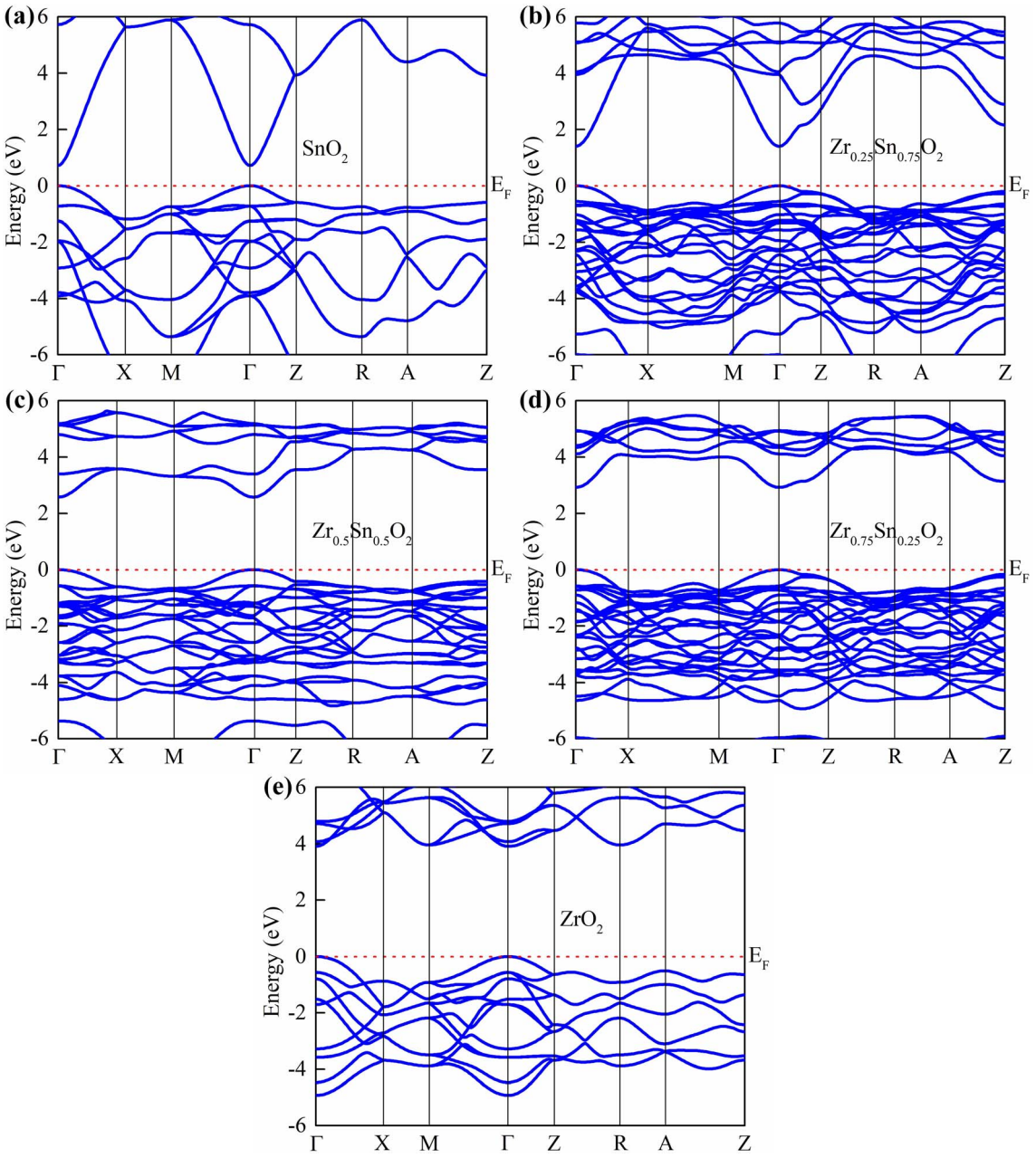

Fig. 4 Band structures along the tetragonal high-symmetry directions for (a) SnO_2, (b) $Zr_{0.25}Sn_{0.75}O_2$, (c) $Zr_{0.5}Sn_{0.5}O_2$, (d) $Zr_{0.75}Sn_{0.25}O_2$, and (e) ZrO_2 calculated at the GGA+U level. The red dotted line is the Fermi level and has been set to zero.

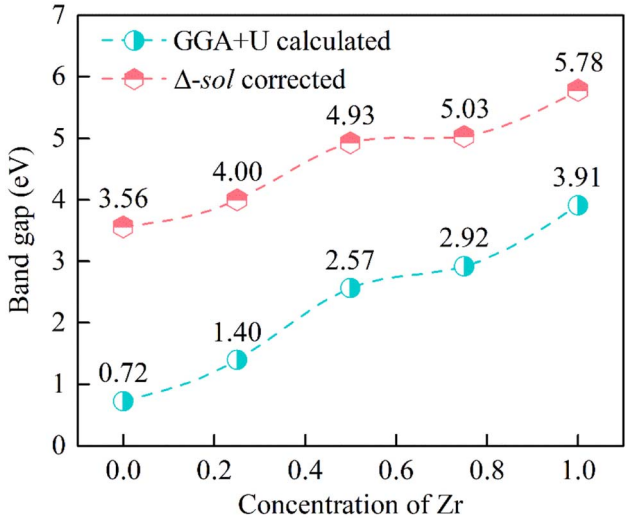

Fig. 5 GGA+U calculated (cyan circle) and Δ-sol corrected (red hexagon) bandgaps as functions of Zr compositions for $Zr_xSn_{1-x}O_2$ alloys.

because the former has stronger locality. In addition, the CBMs are more dispersive than the VBMs, which means that the effective masses of electrons in the conduction bands are smaller than those of holes in the valence bands. Taking the band structure of $Zr_{0.25}Sn_{0.75}O_2$ as an example, we calculated the effective masses of holes in the VBM and electron in the CBM according to the formula $\frac{1}{m} = \frac{1}{\hbar}\frac{\partial^2 E(k)}{\partial k^2}$. The calculated effective masses of electrons and holes are 0.44 m_0 and 3.50 m_0 (m_0 is the mass of an electron), respectively, which confirms that the holes in the valence bands are heavier than the electrons in the conduction bands. Hence, the holes have lower mobility than the electrons. These band structure characteristics also indicate that the O-2p electrons, which form the VBM states (as shown in Fig. 6), are tightly bound to the atoms, reducing the mobility of valence band holes. Thus, although the concentration of conduction band electrons is lower than that of valence band holes, the contribution of electrons to conductivity is greater.

The underestimations of bandgaps by GGA+U method can be attributed to the inherent self-interaction error and the absence of derivative discontinuity in the exchange–correlation potential.[30] To address these issues and diminish discrepancies in the Kohn–Sham energy gap, we implemented the efficient Δ-sol method[31] as a correction measure for GGA+U computed bandgaps. The Δ-sol method can significantly improve Kohn–Sham bandgap errors. It estimates the bandgaps of multicomponent alloys by fitting the experimental bandgap values of pure binary compounds, avoiding complex calculations and reducing computational costs. The Δ-sol method has been successfully applied to calculate the bandgaps of various alloy systems.[15,16,32] The corrected bandgap is within the range of 3.56 to 5.78 eV, as shown in Fig. 5. This indicates that Zr doping is expected to regulate the bandgap of SnO_2 to the deep UV region, so as to realize the application of SnO_2-based ultra-wide bandgap solar-blind deep UV photoelectronic devices.

The projected density of states (PDOS) analysis (Fig. 6) shows that before doping with Zr element, the valence and conduction bands near the Fermi level are mainly contributed by the O-2p and Sn-5s states, respectively. After doping with Zr element, the conduction band near the Fermi level is dominated by Zr-4d states, accompanied by some contributions from Sn-5s states. The effect of Zr-4d states on CBM is greater, so the change in band gap value of $Zr_xSn_{1-x}O_2$ alloy is mainly caused by Zr doping content. Due to the delocalization of the d-band by GGA exchange–correlation potential, the overlap between the O-2p state and the Sn/Zr-4d state is overestimated, resulting in a severely underestimated bandgap in strongly correlated electronic systems.[33] For the conduction band, the lowest unoccupied state near the Fermi level is a mixed state of Sn-5s and Zr-4d. The hybridization of s–d orbitals in the conduction band depends on the relative orbital energies. In fact, the energy difference between the Sn-5s and Zr-4d levels is significant, so as the Zr content increases, the s–d hybridization effect weakens, causing the CBM to move upwards. Therefore, the bandgap of $ZrSnO_2$ alloy gradually widens with the increase of Zr content.

3.2.2. Band offsets. Since Zr doping is bound to affect the electron filling in the VBM and CBM of SnO_2, resulting in changes in the position of VBM and CBM. The band offset can intuitively reflect the relative variation of the band alignment of VBM and CBM at the interface of $Zr_xSn_{1-x}O_2$ alloys with doping content. It is an crucial parameter for evaluating charge transfer, quantum confinement, and conversion efficiency, and is closely related to the design of optoelectronic devices.[22] Therefore, in order to apply $Zr_xSn_{1-x}O_2$ alloys as heterojunctions in electronic and optoelectronic devices, the band offsets of VBM and CBM at the interface of $Zr_xSn_{1-x}O_2$ alloys with different Zr concentrations were calculated, as show in Fig. 7. The valence band offsets are large, while the conduction band offsets are relatively small. In the tetragonal $Zr_xSn_{1-x}O_2$ alloys with T_d site symmetry, the anionic 2p and cationic 4d orbitals are equivalent symmetric states, both of which are transformed into Γ_{15} representation.[34,35] The interaction between them generates energy level repulsion, leading to an increase in valence band offset. Due to the higher energy of Zr-4d orbital compared to Sn-4d orbital, as the Zr content increases, the p–d coupling effect becomes more pronounced, leading to a gradual increase in valence band offset.

3.2.3. Chemical bonding analysis. From the electron localization function (ELF)[36–39] and charge density difference plots (as shown in Fig. 8), it can be seen that there is no charge distribution between metals, which indicates that no bonding interaction exists between them. However, there is a significant amount of charge distribution between the metal and O atoms, and the charge around the metal and O atoms is distributed spherically, indicating that the Sn–O and Zr–O bonds are mainly ionic interactions. According to the Bader charge distribution analysis[40–42] (as listed in Table 2), the Bader charges on Sn, Zr, and O atoms are −2.34 to −2.31 $|e|$, −2.59 to −2.55 $|e|$, and 1.17–1.27 $|e|$, respectively. It indicates that Sn and Zr lose electrons, while O gains electrons and charges transfer from Sn and Zr

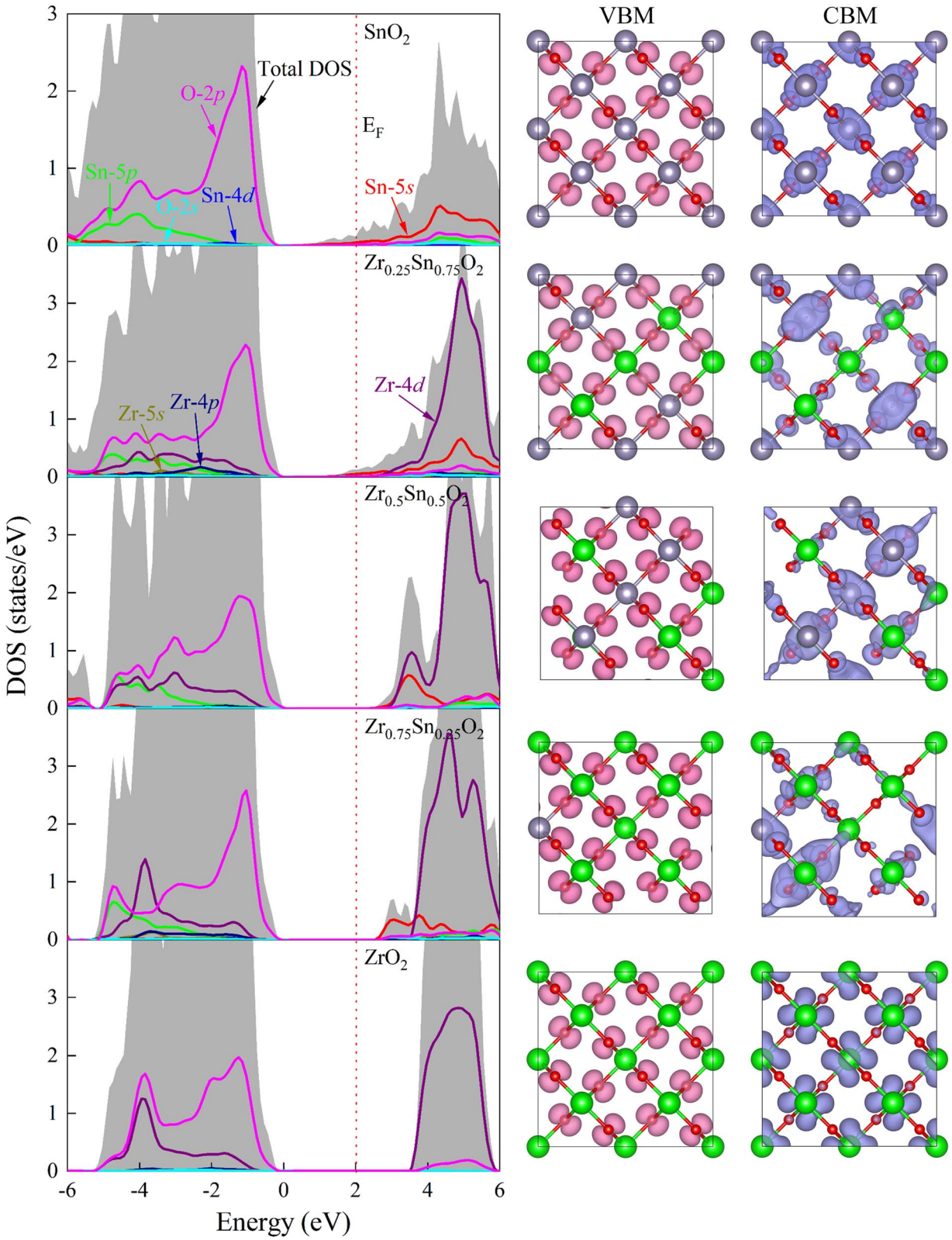

Fig. 6 Projected density of states (PDOS) and band decomposed charge density distribution of VBM and CBM at Γ point for $Zr_xSn_{1-x}O_2$ alloys. The PDOS have been normalized according to the number of atoms in the $Zr_xSn_{1-x}O_2$ alloys to better show how it varies with the Zr composition. The red dotted line is the Fermi level and has been set to zero. The isosurface value is 0.01 e $Å^{-3}$.

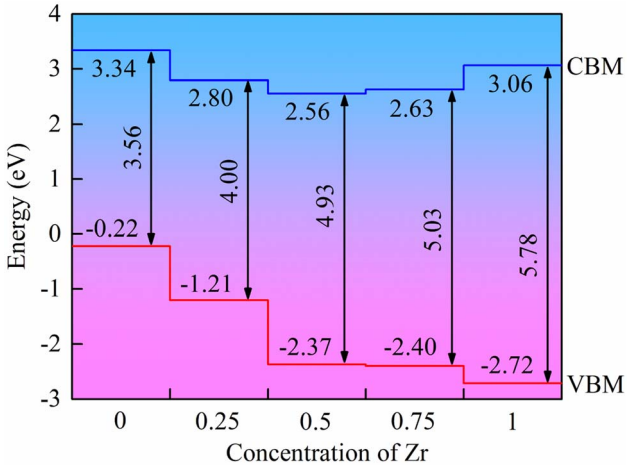

Fig. 7 Band offsets of $Zr_xSn_{1-x}O_2$ alloys with different Zr compositions. The branch-point energies are set to zero, treated as reference energy levels, and used to align the conduction and valence band edges.

Table 2 The Bader charges of Sn, Zr, and O atoms in $Zr_xSn_{1-x}O_2$ alloys. Positive and negative values represent the gain and loss of electrons, respectively

$Zr_xSn_{1-x}O_2$	Sn	Zr	O
0	−2.34	—	1.17
0.25	−2.32	−2.59	1.19
0.5	−2.31	−2.57	1.22
0.75	−2.31	−2.56	1.25
1	—	−2.55	1.27

atoms to O atoms. This is consistent with the phenomenon reflected on the charge density difference plots (Fig. 8d–f).

3.3. Optical properties

The effective response of semiconductor materials to light is vital for their applications in optoelectronic and photovoltaic devices. The optical absorption coefficients of $Zr_xSn_{1-x}O_2$ alloys were calculated based on the imaginary part of the frequency dependent complex dielectric function. As shown in Fig. 9, the

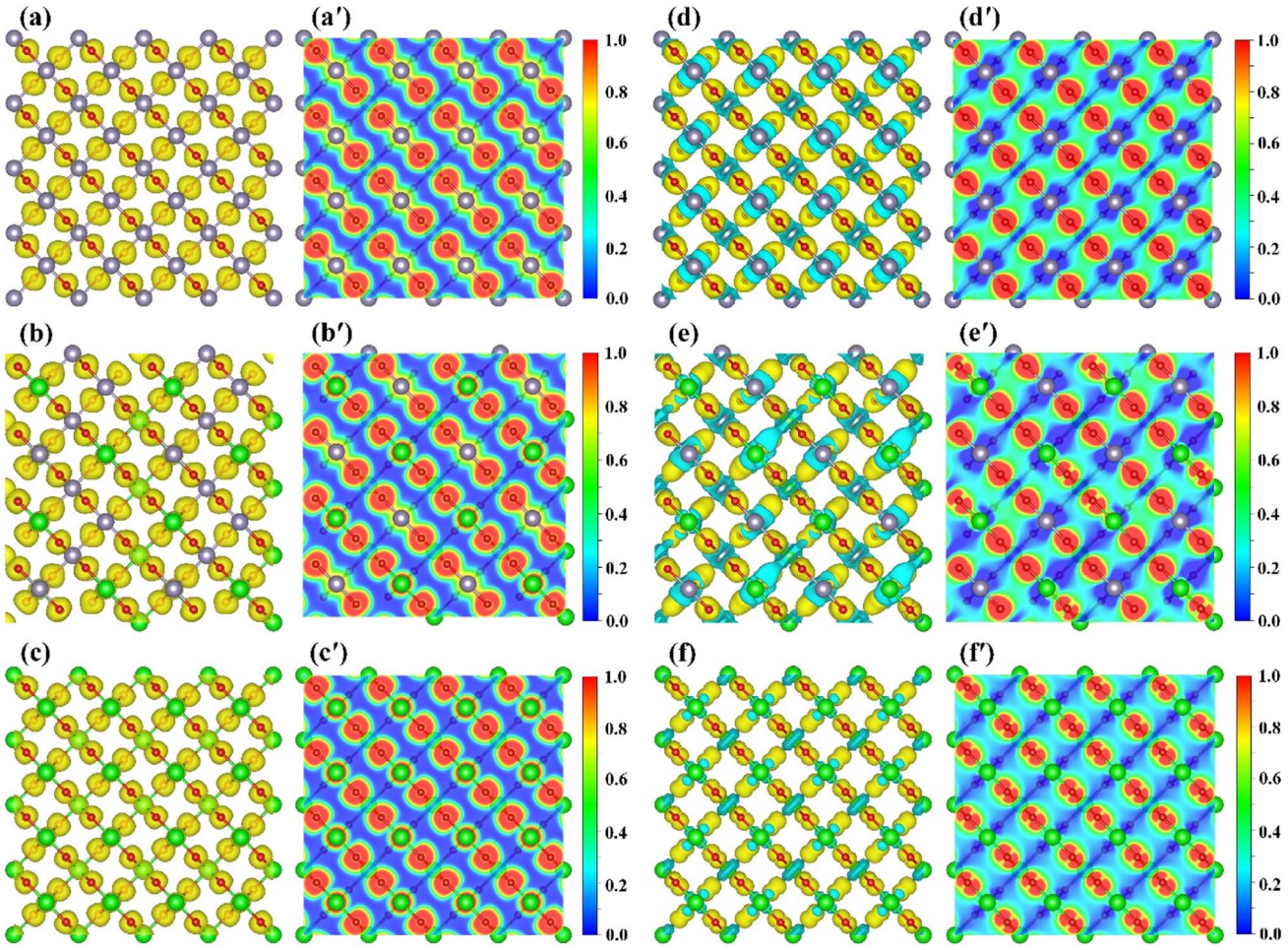

Fig. 8 Calculated ELF of (a) SnO_2, (b) $Zr_{0.5}Sn_{0.5}O_2$, and (c) ZrO_2 alloys in 2 × 2 × 2 supercells at an isosurface value of 0.7 e Å^{-3}. (a′)–(c′) are the sectional plots of corresponding ELF along the (001) plane in (a)–(c). Charge density difference of (d) SnO_2, (e) $Zr_{0.5}Sn_{0.5}O_2$, and (f) ZrO_2 alloys in 2 × 2 × 2 supercells at an isosurface value of 0.01 e Å^{-3}. The yellow and blue bubbles indicate charge accumulation and depletion, respectively. (d′)–(f′) are the sectional plots of corresponding charge density differences along the (001) plane in (d)–(f).

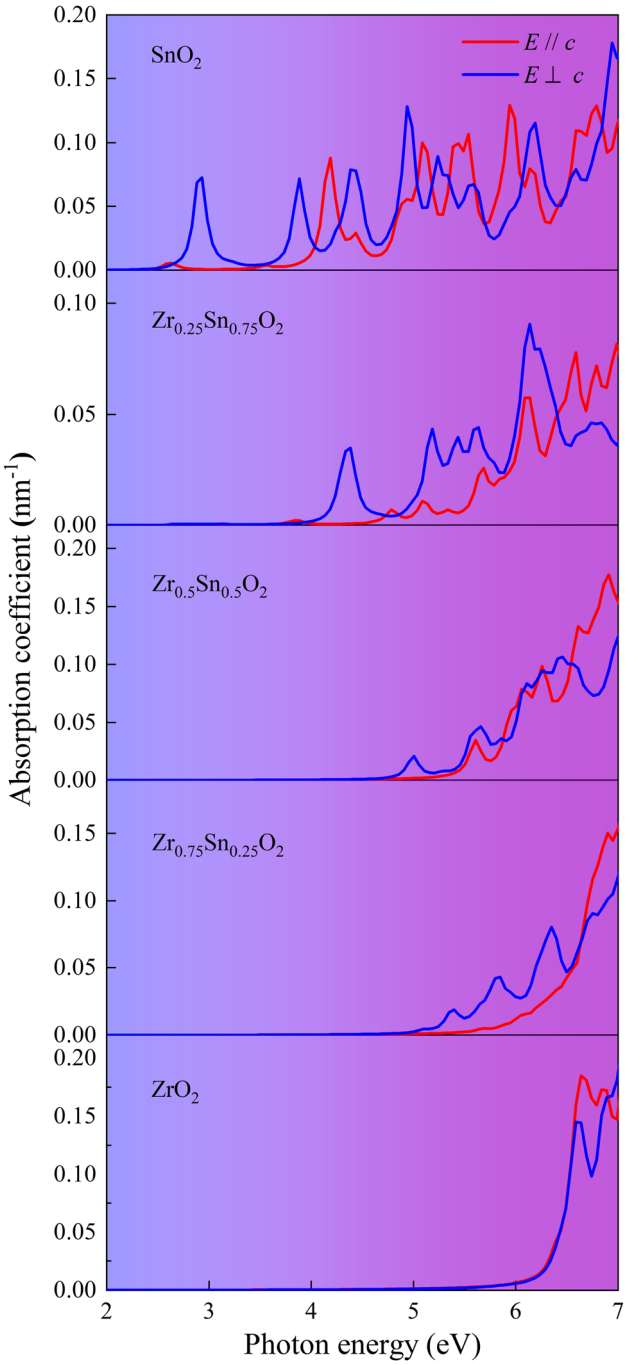

Fig. 9 Absorption coefficients of $Zr_xSn_{1-x}O_2$ alloys with different Zr compositions for parallel (red) and perpendicular (blue) light polarization.

absorption coefficients of $Zr_xSn_{1-x}O_2$ alloys exhibit significant optical anisotropy. The absorption edge of pure SnO_2 is located in the UV-B spectrum range, with the shortest cutoff wavelength of about 320 nm, which can only achieve visible light- blind UV detection. After the incorporation of Zr element, the adsorption edge shows a notable blue shift. As the Zr content increases from 0 to more than 25%, the absorption edge of the $ZrSnO_2$ alloy gradually shifts to the deep UV region. This is expected to enable the application of solar-blind deep UV photodetectors.

4. Conclusions

The positive formation enthalpies of $Zr_xSn_{1-x}O_2$ alloys indicate that it is difficult for SnO_2 and ZrO_2 to form stable and ordered solid solutions. They show a tendency of phase separation at low temperatures, but may form good disordered alloys at high temperatures. The ultra-wide $Zr_xSn_{1-x}O_2$ semiconductor alloys may achieve a full-component solid solution above the critical temperature of 979 K. Through band engineering, the bandgap of $ZrSnO_2$ alloy varies from 3.56 to 5.78 eV. It is expected to realize the preparation of SnO_2-based ultra-wide bandgap semiconductor alloys, so as to achieve the application of solar-blind deep UV photoelectronic devices. The increase of Zr content weakens the s–d hybridization effect, which leads to the upward movement of the CBM, thus widening the bandgap of $ZrSnO_2$ alloy. Since the Zr-4d orbital has higher energy than the Sn-4d orbital, the p–d coupling effect becomes more obvious with the increase of Zr content, resulting in a gradual increase in the valence band offset. As the Zr content exceeds 25%, the absorption edge of $ZrSnO_2$ alloy moves to the deep UV region, which is expected to realize the application of solar-blind deep UV photodetectors.

Conflicts of interest

The authors declare no competing financial interest.

Acknowledgements

This work was supported by the Natural Science Foundation of Xiaogan City (Grant No. XGKJ2022010105), the Hubei Province Young Science and Technology Talent “Morning Light Lift” Project, and the Project of the Hubei Provincial Department of Education (No. T201617).

References

1 W. Zhang, M. Xu, M. Zhang, H. Cheng, M. Li, Q. Zhang, Y. Lu, J. Chen, C. Chen and Y. He, Pulsed laser deposited $Be_xZn_{1-x}O_{1-y}S_y$ quaternary alloy films: structure, composition, and band gap bowing, *Appl. Surf. Sci.*, 2018, **433**, 674–679.

2 M. Zhang, M. Xu, M. Li, Q. Zhang, Y. Lu, J. Chen, M. Li, J. Dai, C. Chen and Y. He, SnO_2 epitaxial films with varying thickness on *c*-sapphire: structure evolution and optical band gap modulation, *Appl. Surf. Sci.*, 2017, **423**, 611–618.

3 Y. M. Lu, J. Jiang, M. Becker, B. Kramm, L. Chen, A. Polity, Y. B. He, P. J. Klar and B. K. Meyer, Polycrystalline SnO_2 films grown by chemical vapor deposition on quartz glass, *Vacuum*, 2015, **122**, 347–352.

4 Y. H. Liang and E. Towe, Progress in efficient doping of high aluminum-containing group III-nitrides, *Appl. Phys. Rev.*, 2018, **5**(1), 011107.

5 S. J. Pearton, J. Yang, P. H. I. V. Cary, F. Ren, J. Kim, M. J. Tadjer and M. A. Mastro, A review of Ga_2O_3 materials, processing, and devices, *Appl. Phys. Rev.*, 2018, **5**(1), 011301.

6 T. Luo, G. Ye, X. Chen, H. Wu, W. Zhang and H. Chang, F-doping-enhanced carrier transport in the SnO_2/perovskite interface for high-performance perovskite solar cells, *ACS Appl. Mater. Interfaces*, 2022, **14**(37), 42093–42101.

7 P. Wu, S. Wang, X. Li and F. Zhang, Advances in SnO_2-based perovskite solar cells: from preparation to photovoltaic applications, *J. Mater. Chem. A*, 2021, **9**(35), 19554–19588.

8 H. Zhou, R. Deng, Y.-F. Li, B. Yao, Z.-H. Ding, Q.-X. Wang, Y. Han, T. Wu and L. Liu, Wavelength-tuned light emission via modifying the band edge symmetry: doped SnO_2 as an example, *J. Phys. Chem. C*, 2014, **118**(12), 6365–6371.

9 M. Rouchdi, E. Salmani, A. El hat, C. Nassiri, N. Hassanain and A. Mzerd, Synthesis and magnetic properties of Mg doped SnO_2 thin films: experimental and Ab-initio study, *Opt. Quantum Electron.*, 2017, **49**(4), 150.

10 H. He, Z. Xie, Q. Li, J. Li and Q. Zhang, Novel p-type conductivity in SnO_2 thin films by Mg doping, *J. Alloys Compd.*, 2017, **714**, 258–262.

11 C. Ling, T. Guo, W. Lu, Y. Xiong, L. Zhu and Q. Xue, Ultrahigh broadband photoresponse of SnO_2 nanoparticle thin film/SiO_2/p-Si heterojunction, *Nanoscale*, 2017, **9**(25), 8848–8857.

12 A. van de Walle, M. Asta and G. Ceder, The alloy theoretic automated toolkit: a user guide, *Calphad*, 2002, **26**(4), 539–553.

13 D. Long, M. Li, D. Meng, Y. He, I. T. Yoon, R. Ahuja and W. Luo, Accounting for the thermo-stability of PdH_x (x = 1–3) by density functional theory, *Int. J. Hydrogen Energy*, 2018, **43**(39), 18372–18381.

14 M. Li, D. Long, R. Ahuja and Y. He, Magnetic order and phase diagram of magnetic alloy system: $Mg_xNi_{1-x}O$ alloy, *Phys. Status Solidi B*, 2017, **254**(9), 1700085.

15 D. Long, M. Li, D. Meng, R. Ahuja and Y. He, Theoretical investigation of the structural, electronic, and thermodynamic properties of $CdS_{1-x}Se_x$ alloys, *J. Appl. Phys.*, 2018, **123**(10), 105103.

16 D. Long, M. Li, D. Meng and Y. He, Electronic-structure and thermodynamic properties of $ZnS_{1-x}Se_x$ ternary alloys from the first-principles calculations, *Comput. Mater. Sci.*, 2018, **149**, 386–396.

17 P. Giannozzi, S. Baroni, N. Bonini, M. Calandra, R. Car, C. Cavazzoni, D. Ceresoli, G. L. Chiarotti, M. Cococcioni, I. Dabo, A. Dal Corso, S. de Gironcoli, S. Fabris, G. Fratesi, R. Gebauer, U. Gerstmann, C. Gougoussis, A. Kokalj, M. Lazzeri, L. Martin-Samos, N. Marzari, F. Mauri, R. Mazzarello, S. Paolini, A. Pasquarello, L. Paulatto, C. Sbraccia, S. Scandolo, G. Sclauzero, A. P. Seitsonen, A. Smogunov, P. Umari and R. M. Wentzcovitch, QUANTUM ESPRESSO: a modular and open-source software project for quantum simulations of materials, *J. Phys.: Condens. Matter*, 2009, **21**(39), 395502.

18 K. F. Garrity, J. W. Bennett, K. M. Rabe and D. Vanderbilt, Pseudopotentials for high-throughput DFT calculations, *Comput. Mater. Sci.*, 2014, **81**, 446–452.

19 J. P. Perdew, K. Burke and M. Ernzerhof, Generalized gradient approximation made simple, *Phys. Rev. Lett.*, 1996, **77**(18), 3865–3868.

20 J. Wang, G. Li, Z. Li, C. Tang, Z. Feng, H. An, H. Liu, T. Liu and C. Li, A highly selective and stable ZnO-ZrO_2 solid solution catalyst for CO_2 hydrogenation to methanol, *Sci. Adv.*, 2017, **3**(10), e1701290.

21 N. Igawa and Y. Ishii, Crystal structure of metastable tetragonal zirconia up to 1473 K, *J. Am. Ceram. Soc.*, 2001, **84**(5), 1169–1171.

22 A. Schleife, F. Fuchs, C. Rödl, J. Furthmüller and F. Bechstedt, Branch-point energies and band discontinuities of III-nitrides and III-/II-oxides from quasiparticle band-structure calculations, *Appl. Phys. Lett.*, 2009, **94**(1), 012104.

23 P. Li, C.-W. Zhang, J. Lian, M.-J. Ren, P.-J. Wang, X.-H. Yu and S. Gao, First-principle study of optical properties of Cu-doped CdS, *Opt. Commun.*, 2013, **295**, 45–52.

24 P. Y. Yu and M. Cardona, *Fundamentals of Semiconductors*, Springer, Berlin, 1996, pp. 1991–1639.

25 S. Saha, T. P. Sinha and A. Mookerjee, Electronic structure, chemical bonding, and optical properties of paraelectric $BaTiO_3$, *Phys. Rev. B: Condens. Matter Mater. Phys.*, 2000, **62**(13), 8828–8834.

26 R. H. T. Yeh, Composite Ising lattices. I. Bragg-Williams approximation, *Phys. Rev. B: Solid State*, 1970, **1**(3), 1180–1183.

27 N. N. K. Reddy, H. S. Akkera, M. C. Sekhar and S.-H. Park, Zr-doped SnO_2 thin films synthesized by spray pyrolysis technique for barrier layers in solar cells, *Appl. Phys. A*, 2017, **123**(12), 761.

28 D.-S. Han, J.-H. Park, Y.-J. Kang and J.-W. Park, Effects of zirconium doping on the characteristics of tin oxide thin film transistors, *Microelectron. Reliab.*, 2013, **53**(12), 1875–1878.

29 P. Ye, M. Li, W. Fu, H. Wei, W. E, X. Xiao and Y. He, Nb-doped $Zr_xSn_{1-x}O_2$: experimental and first-principles study, *J. Appl. Phys.*, 2021, **130**(1), 015702.

30 A. Seidl, A. Görling, P. Vogl, J. A. Majewski and M. Levy, Generalized Kohn-Sham schemes and the band-gap problem, *Phys. Rev. B: Condens. Matter Mater. Phys.*, 1996, **53**(7), 3764–3774.

31 M. K. Y. Chan and G. Ceder, Efficient band gap prediction for solids, *Phys. Rev. Lett.*, 2010, **105**(19), 196403.

32 P. Scharoch and M. Winiarski, An efficient method of DFT/LDA band-gap correction, *Comput. Phys. Commun.*, 2013, **184**(12), 2680–2683.

33 I. Khan, I. Ahmad, H. A. R. Aliabad, S. J. Asadabadi, Z. Ali and M. Maqbool, Conversion of optically isotropic to anisotropic CdS_xSe_{1-x} ($0 \nleqq x \nleqq 1$) alloy with S concentration, *Comput. Mater. Sci.*, 2013, **77**, 145–152.

34 S.-H. Wei and A. Zunger, Role of d orbitals in valence-band offsets of common-anion semiconductors, *Phys. Rev. Lett.*, 1987, **59**(1), 144–147.

35 S. H. Wei and A. Zunger, Role of metal d states in II-VI semiconductors, *Phys. Rev. B: Condens. Matter Mater. Phys.*, 1988, **37**(15), 8958–8981.

36 A. D. Becke and K. E. Edgecombe, A simple measure of electron localization in atomic and molecular systems, *J. Chem. Phys.*, 1990, **92**(9), 5397–5403.

37 A. Savin, R. Nesper, S. Wengert and T. F. Fässler, ELF: the electron localization function, *Angew Chem. Int. Ed. Engl.*, 1997, **36**(17), 1808–1832.
38 P. Fuentealba, E. Chamorro and J. C. Santos, Chapter 5 Understanding and using the electron localization function, in *Theoretical and Computational Chemistry*, ed. A. Toro-Labbé, Elsevier, 2007, vol. 19, pp. 57–85.
39 Y. Grin, A. Savin and B. Silvi, The ELF perspective of chemical bonding, in *The Chemical Bond*, 2014, pp. 345–382.
40 G. Henkelman, A. Arnaldsson and H. Jónsson, A fast and robust algorithm for Bader decomposition of charge density, *Comput. Mater. Sci.*, 2006, **36**(3), 354–360.
41 E. Sanville, S. D. Kenny, R. Smith and G. Henkelman, Improved grid-based algorithm for Bader charge allocation, *J. Comput. Chem.*, 2007, **28**(5), 899–908.
42 W. Tang, E. Sanville and G. Henkelman, A grid-based Bader analysis algorithm without lattice bias, *J. Phys.: Condens. Matter*, 2009, **21**(8), 084204.